Research Article | Vol. 29, No. 26 / 20 Dec 2021 / Optics Express 44283
Optics EXPRESS

Three-dimensional hologram calculations using blocked radial and windmill point spread functions

DAIKI YASUKI,[1] TOMOYOSHI SHIMOBABA,[1,*] MICHAL MAKOWSKI,[2] DAVID BLINDER,[3,4] JAROSLAW SUSZEK,[2] MACIEJ SYPEK,[2] TOBIAS BIRNBAUM,[3,4] PETER SCHELKENS,[3,4] TAKASHI KAKUE,[1] AND TOMOYOSHI ITO[1]

[1]*Graduate School of Engineering, Chiba University, 1-33 Yayoi, Inage, Chiba 263-8522, Japan*
[2]*Faculty of Physics, Warsaw University of Technology, Koszykowa 75, Warsaw 00-662, Poland*
[3]*Department of Electronics and Informatics (ETRO), Vrije Universiteit Brussel, Pleinlaan 2, B-1050 Brussel, Belgium*
[4]*IMEC, Kapeldreef 75, B-3001 Leuven, Belgium*
[*]*shimobaba@faculty.chiba-u.jp*

Abstract: Holograms are computable by superimposing zone-plate-like point spread functions (PSFs), representing the distribution of light on the hologram plane. However, due to the computational cost of large-scale holograms, it is difficult to compute them at video rates for high-definition holographic displays. Recently, we proposed radial PSFs for holographic near-eye displays [Appl. Opt.**60**, 8829-8837, (2021).]. Radial PSFs can speed-up hologram computations for fixed viewpoints, but they are unsuitable for naked-eye displays with wide viewing angles because of the reduced information in the PSFs. This study proposes blocked radial PSFs, which can accelerate computations with radial PSFs, and windmill PSFs (rotational radial PSFs). Both can be applied easily to holographic displays with wide viewing angles.

1. Introduction

Computer-generated holograms (CGHs) are a technology for synthesizing holograms on a computer, and by displaying CGHs on a spatial light modulator (SLM); it is possible to reconstruct three-dimensional (3D) images that are comfortable for human stereoscopic perception [1–3]. Hologram-computation algorithms are mainly classified into point-cloud methods [4–16], polygon methods [17–19], light-field methods [20–23], and layer methods [24–26]. In addition, in recent years, deep learning has been used to infer CGHs directly [27–30]. In this study, we focus on point-cloud methods. In those methods, CGHs can be calculated by superimposing point spread functions (PSFs) that represent the light distribution on the CGH plane. Due to their simple principles, point-cloud methods also can be applied flexibly to polygon, light-field, and layer methods. CGH computations based on deep learning currently deal mainly with layer methods, targeting holographic displays with fixed observing positions (e.g., near-eye displays) [31–37]. It is worthwhile to speed-up computations of point-cloud methods so that they can be applied to holographic displays with wider viewing angles in addition to near-eye displays.

The PSFs used in holographic displays have wide viewing areas, typically designed to observe the reconstructed image from any angle, resulting in dense, zone-plate-like light distribution. In this study, we call such a PSF an "entire PSF." On the other hand, holographic near-eye displays do not need to calculate the distribution of all the light, as is done with entire PSFs, because the position of the viewpoint is fixed. By reducing the PSF light distribution computation to eliminate light that is unnecessary for observation, we can thus speed up the CGH calculations.

#447737 https://doi.org/10.1364/OE.447737
Journal © 2021 Received 5 Nov 2021; revised 2 Dec 2021; accepted 6 Dec 2021; published 17 Dec 2021

Optics EXPRESS

We have proposed three types of PSFs for near-eye displays: PSFs with horizontal parallax only, cross PSFs, and radial PSFs [16]. Simulations and optical experiments have shown that images reconstructed using radial PSFs are almost equal in image quality and depth of focus to images reconstructed using entire PSFs [16]. Radial PSFs have a sparse optical distribution than entire PSFs; thus, CGHs can be calculated faster. Radial PSFs can produce correctly reconstructed images under the condition that the viewpoint is fixed, as is the case for near-eye displays. However, when PSFs are applied to holographic displays with wide viewing angles, part of the reconstructed image may be missing when the eye position is moved. In addition, the structures of radial PSFs make it difficult to apply them to fast algorithms that compute CGHs by dividing them into blocks, such as the phase-added stereogram (PAS) algorithm [11–15].

In this study, we propose two PSFs to solve these problems. One is a blocked radial PSF. The other is a rotational blocked radial PSF, which can be applied to holographic displays with wide viewing angles by calculating holograms while rotating the blocked radial PSFs. We call rotated-blocked-radial PSFs "windmill PSFs" because they look like the rotating blades of a windmill. In this study, we employ these PSFs with the wavefront-recording-plane (WRP) method [8] and the PAS algorithm [11–15], and we evaluate their calculation speeds and image quality. In section 2, we describe blocked radial PSFs and windmill PSFs. In section 3, we evaluate the calculation speed and image quality of CGH computations using either the conventional or the proposed PSFs, and we display numerical and optical reconstructions. Finally, we summarize this work and provide future perspectives in section 4.

2. Proposed point spread functions: blocked radial PSF and windmill PSF

First, we summarize the fast computation algorithms for holograms used in this study. We describe the proposed PSFs—the blocked radial PSF and the windmill PSF—subsequently.

2.1. Fast computation algorithms for holograms

CGHs can be generated by superimposing PSFs, representing the light-wave distribution on the hologram plane of spherical waves emitted from object points. The complex hologram, H, in the CGH plane can be written as

$$H(x_h, y_h) = \sum_{j=1}^{M} A_j \exp\left(i\frac{2\pi}{\lambda} r_{hj}\right) = \sum_{j=1}^{M} A_j u_{z_j}(x_h - x_j,\ y_h - y_j\ ), \tag{1}$$

where i is the imaginary unit, M is the number of object points, λ is the wavelength, (x_h, y_h) are the coordinates in the CGH plane, (x_j, y_j, z_j) are the coordinates of the j-th object point, A_j is the amplitude of the j-th object point, u_{z_j} is the entire PSF at z_j, and r_{hj} is the distance between an object point and a pixel in the CGH plane. The entire PSF can then be written as

$$u_{zj} = \exp\left(i\frac{2\pi}{\lambda} r_{hj}\right) \approx \exp\left(i\frac{2\pi}{\lambda}\left(z_j + \frac{(x_h - x_j)^2 + (y_h - y_j)^2}{2z_j}\right)\right). \tag{2}$$

If the resolution of the CGH is $N \times N$, the computational cost of the CGH calculation expressed by Eq. (1) is $O(N^2M)$. In this calculation, the superposition of PSFs is particularly time-consuming. The Look-Up Table (LUT) method [4–7], the WRP method [8], and the PAS algorithm [11–15] might solve this problem.

The LUT method reduces the computational cost by precomputing the PSFs in Eq. (1) and storing them in the LUT. The WRP method introduces a virtual plane (the WRP) between the object and the CGH and records the light from the object that falls onto the virtual plane using Eq. (1). One then obtains the CGH by calculating the light propagation from the virtual plane to

Optics EXPRESS

the CGH. We place the WRP close to the object being recorded, so the PSF radius in the WRP is small, reducing the CGH computational complexity.

The PAS algorithm divides the CGH into small blocks of dimensions $B \times B$ and approximates the PSF of each block by a plane wave. A single spectrum in the frequency domain can represent the plane wave, which speeds up the CGH calculation. After the plane-wave spectra of all the object points are superimposed in the frequency domain, the inverse Fourier transform for each block is calculated to generate the hologram. If the frequency resolution is low for a block size of $B \times B$, the frequency domain is extended to a larger size of dimension $S \times S$. After executing the inverse Fourier transform on the extended block, we crop the $B \times B$ block from the extended block and assign it to the corresponding hologram block. The PAS computational complexity is approximately $O\left(\frac{MN^2}{B^2}\right)$, which speeds up the CGH calculation.

2.2. Proposed point spread functions: blocked radial PSF and windmill PSF

Radial PSFs were proposed to generate holograms faster by reducing the distribution of light obtained from entire PSFs without affecting the observation when the viewpoint position is fixed [16]. Figure 1(a) shows an example of a radial PSF; it has a continuous distribution of light waves in the diagonal direction. However, this is incompatible with the PAS algorithm, which divides the CGH into rectangular blocks to achieve fast computation. In addition, the calculation of the diagonal positions of the light waves is troublesome. In this study, we, therefore, propose a blocked radial PSF that solves these problems. The blocked radial PSF is formed from blocks, as shown by the yellow rectangle in Fig. 1(b).

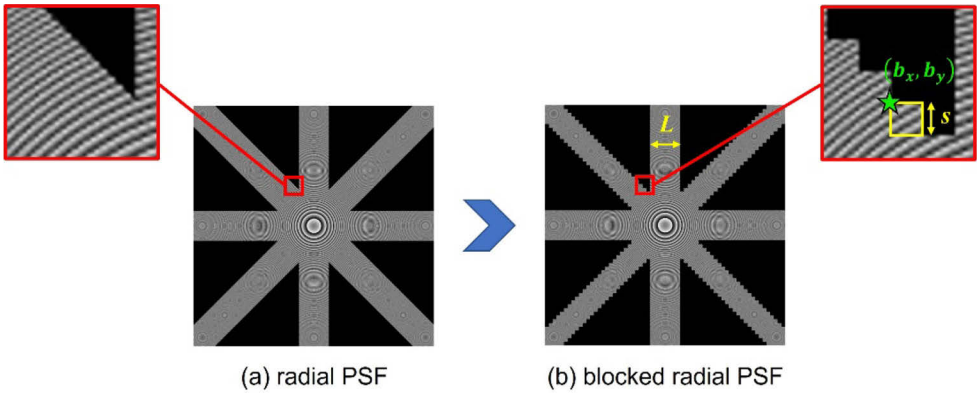

Fig. 1. Radial PSF and blocked radial PSF.

Figure 2 shows an entire PSF, a radial PSF, and the proposed blocked radial PSF together with their focusing properties. The focusing properties refer to the intensity distribution at the focal point of a PSF irradiated with a plane wave.

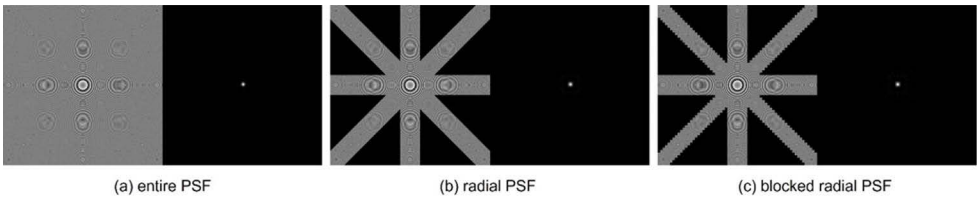

Fig. 2. Entire PSF, radial PSF, and blocked radial PSF.

Optics EXPRESS

By calculating the entire PSF only where a mask function M_b is 1, we can generate a blocked radial PSF. The mask function, M_b, of the blocked radial PSF shown in Fig. 2(c) can be expressed as

$$M_b = \begin{cases} 1, \ if \ case \ M_b \\ 0, \ otherwise \end{cases}, \tag{3}$$

where "case M_b" in Eq. (3) can be expressed as

$$\begin{aligned} &\left|\frac{n_x-1}{2}-\left(b_x-\frac{x_j}{s}\right)\right| \le \alpha \ \wedge \ \left|\frac{n_y-1}{2}-\left(b_y-\frac{y_j}{s}\right)\right| \le \alpha \\ \wedge \ &\left|\beta\left(b_x-\frac{x_j}{s}\right)-\left(b_y-\frac{y_j}{s}\right)\right| \le \alpha \ \wedge \ \left|\beta\left(b_x-\frac{x_j}{s}\right)+\left(b_y-\frac{y_j}{s}\right)-(n_y-1)\right| \le \alpha, \end{aligned} \tag{4}$$

where n_x and n_y are the numbers of blocks on one side of the CGH. As shown in Fig. 1(b), b_x and b_y are the index of the block, s is the size of the block, $\alpha = \frac{L}{2\times s}$ (where L is the width of the blocked radial PSF), and $\beta = \frac{N_y}{N_x}$ (where N_x and N_y are the numbers of pixels in the CGH). By changing L to an arbitrary size, we can change the amount of reduction of the light distribution in the PSF.

Figure 3 shows the images reconstructed from CGHs generated using two of the PSFs in Fig. 2. The number of pixels in the CGH is 2,048 × 2,048, the wavelength is 532 nm, the pixel pitch is 3.74 µm, and the distance between the CGH and the 3D object is 10 cm. We used an Earth model with 30,492 points as the 3D object. The reconstructed images focus on the land in the upper left corner. The edge of the Earth is at the back of the 3D scene. Figure 3(a) is the image reconstructed with the entire PSF. The Earth's edge is out of focus, indicating that the depth of focus is shallow. With the blocked radial PSF, the focusing properties are similar to those of the entire PSF. We subjectively confirmed that the image reconstructed with the blocked radial PSF has image quality and depth of focus close to Fig. 3(a). In Section 3, we will objectively evaluate the image quality.

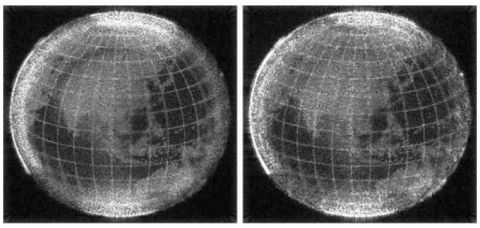

Fig. 3. Images reconstructed using two of the PSFs shown in Fig. 2. We adjusted the contrast to make it easier to see the reconstructed images.

Radial PSFs work well on near-eye displays with a fixed viewpoint. However, when observing an image reconstructed from a holographic display after moving the eye position to a wide viewing angle, the problem occurs that some parts of the reconstructed images are missing. Figure 4(a) shows reconstructed images observed from 2.0° horizontally and −1.0° vertically from the center of the CGH, and Fig. 4(b) shows reconstructed images observed from 2.0° horizontally and +1.0° vertically from the center of the CGH. The number of pixels in the CGH is 8,192 × 8.192, the wavelength is 532 nm, the pixel pitch is 3.74 µm, and the distance between the CGH and the 3D object is 50 cm. We used an Earth model with 30,492 points was used as the 3D object. Compared to the entire PSF, the image reconstructed with the radial PSF has a missing part, and the image contains additional noise.

Optics EXPRESS

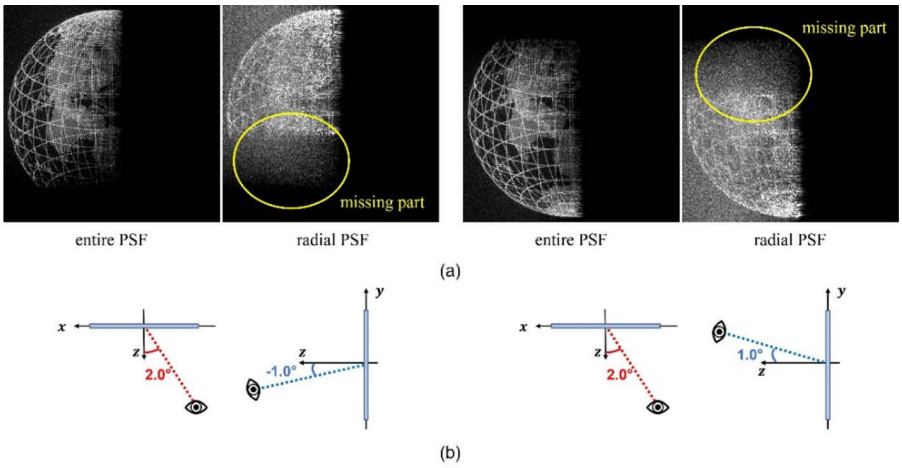

Fig. 4. Image reconstructed from a CGH observed from oblique angles: (a) reconstructed images using the entire and radial PSFs, and (b) schematic diagram of the viewing position. The contrast was adjusted to make it easier to see the reconstructed images.

To solve this problem, we propose a windmill PSF, in which a blocked radial PSF is rotated. Figure 5(a) shows that the windmill PSF gives a blocked radial PSF rotated at a different angle for each adjacent object point. As shown in Fig. 5(b), the radial PSF (and blocked radial PSF) can correctly reconstruct a 3D image for angles where a light distribution exists (viewpoint 2), but a 3D image is not reconstructed from angles where a light distribution does not exist (viewpoint 1), so the 3D image observed from this angle is not reconstructed correctly. In contrast, as shown in Fig. 5(c), the windmill PSF rotates the blocked radial PSF for each object point, so if the object points are dense, they are averaged and the PSF becomes like the entire PSF. Therefore, one of the rays will be visible in viewpoints 1 and 2. As a result, the windmill PSF can reduce the loss of the reconstructed image compared to the radial PSF (and blocked radial PSF).

By calculating the entire PSF only where a mask function M_w is 1, we can generate a windmill PSF:

$$M_w = \begin{cases} 1, \ if \ \left|\frac{n_x-1}{2} - r_x\right| \le \alpha \wedge \left|\frac{n_y-1}{2} - r_y\right| \le \alpha \wedge |\beta r_x - r_y| \le \alpha \wedge |\beta r_x + r_y - (n_y-1)| \le \alpha \\ 0, \ otherwise \end{cases}. \tag{5}$$

Here, r_x and r_y can be written as

$$\begin{pmatrix} r_x - \frac{n_x-1}{2} \\ r_y - \frac{n_y-1}{2} \end{pmatrix} = \mathbb{R}(\theta) \begin{pmatrix} b_x - \frac{x_j}{s} - \frac{n_x-1}{2} \\ b_y - \frac{y_j}{s} - \frac{n_y-1}{2} \end{pmatrix} \tag{6}$$

where θ is the rotation angle of the windmill PSF and $\mathbb{R}(\theta) = \begin{pmatrix} \cos\theta & -\sin\theta \\ \sin\theta & \cos\theta \end{pmatrix}$.

We preliminary investigated the rotation angle θ of the windmill PSF. We first evaluated six different rotation angles for the windmill PSF: 10°, 15°, 20°, 25°, 30°, and a random rotation. When calculating the next object point with a fixed rotation angle (10°, 15°, 20°, 25°, and 30°), we use the new windmill PSF by adding the fixed angle to its previous angle. In the case of random rotation, the windmill PSF of each object point will be rotated randomly. The resulting

Optics EXPRESS

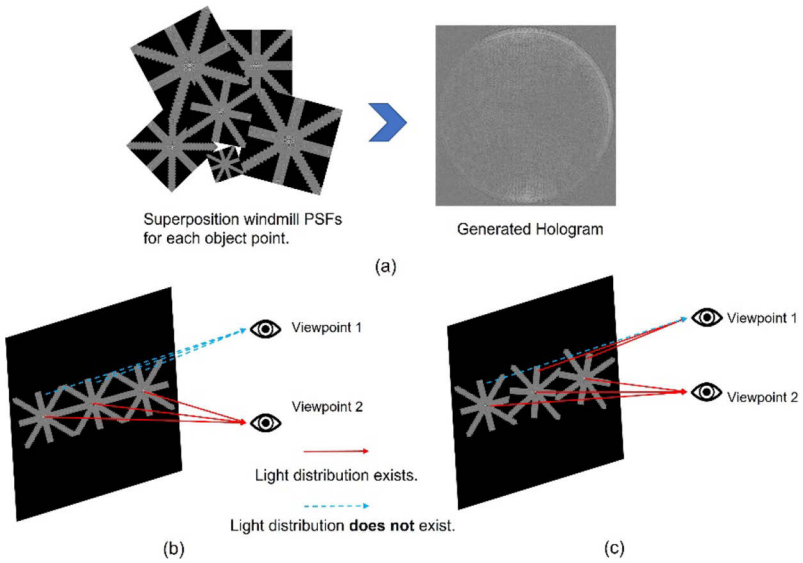

Fig. 5. Outline of a hologram calculation using a windmill PSF: (a) hologram generation using the windmill PSF, (b) radial and blocked radial PSFs in viewpoints 1 and 2 in, and (c) the windmill PSF in viewpoints 1 and 2. The reason why the size of each PSF is different in (a) is that the light spreads differently depending on the distance of the object point. If the object point is close to the hologram, the distribution of PSFs will not spread, and if it is far away, the distribution will spread.

image qualities were almost the same, although the 10° rotation produced slightly better results. We, therefore, used a 10° rotation subsequently.

In addition, the PAS algorithm is calculated by dividing the hologram into blocks and writing the spectrum into each block. In blocked radial PSF and windmill PSF, the hologram is divided into blocks, which makes it easier to apply the PAS algorithm. Since the positions of the blocks are represented by Eqs. (4) and (5), we can calculate the hologram by combining PAS with blocked radial PSF and windmill PSF by writing the spectrum to the blocks. In the PAS calculation, we do not use any LUTs.

3. Results

We next compare the calculation speed and image quality of CGH calculations using the proposed PSFs. We used point-cloud data and RGB–D images as the 3D objects. We used the operating system Windows 10 Enterprise, an Intel Core i7-6700 CPU operating at 3.40 GHz, 16.0 GB of memory, and the Microsoft Visual C++ 2019 compiler. Figure 6 shows the 3D point-cloud data used in this study (the Earth and a merry-go-round). Table 1 shows the CGH calculation parameters. Each object was 2 cm thick, and the sampling interval in the depth direction was 0.2 mm.

Figures 7 and 8 show the images reconstructed from CGHs calculated using the entire PSF, the blocked radial PSF, and the windmill PSF.

Table 2 shows the calculation time when using each PSF. The speed-up factor is calculated as (computation time when using the entire PSF)/(calculation time for each calculation method). Table 2 shows that both the blocked radial PSF and the windmill PSF accelerate the calculation speed further than conventional acceleration methods that use the entire PSF. In particular, when applied to the PAS algorithm, we achieved a speed up of more than 160 fold.

Optics EXPRESS

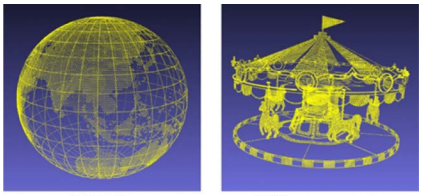

Fig. 6. Original 3D point-cloud data.

Table 1. Calculation parameters for CGH.

Number of pixels	2,048 × 2,048 [pixels]
Pixel pitch	3.74 [μm]
Wavelength	532 [nm]
Number of Object Points	Earth: 30,492 points Merry-go-round: 95,949 points
Distance to CGH	Object thickness 10.0[cm]
Distance to WRP	0.5 [cm]
Line size (L)	256 [pixel]
Block size (s)	32 × 32 [pixels]

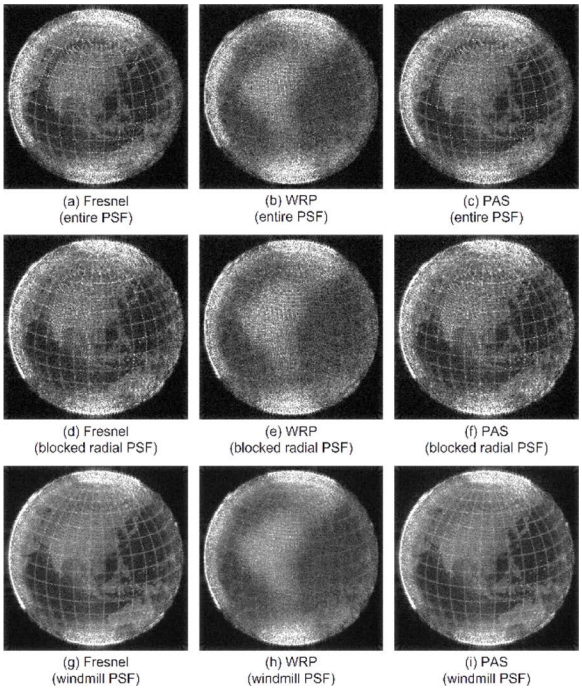

Fig. 7. Reconstructed images. (Object: Earth; reconstruction distance 10.20 cm from the CGHs). We adjusted the contrast to make it easier to see the reconstructed images.

Optics EXPRESS

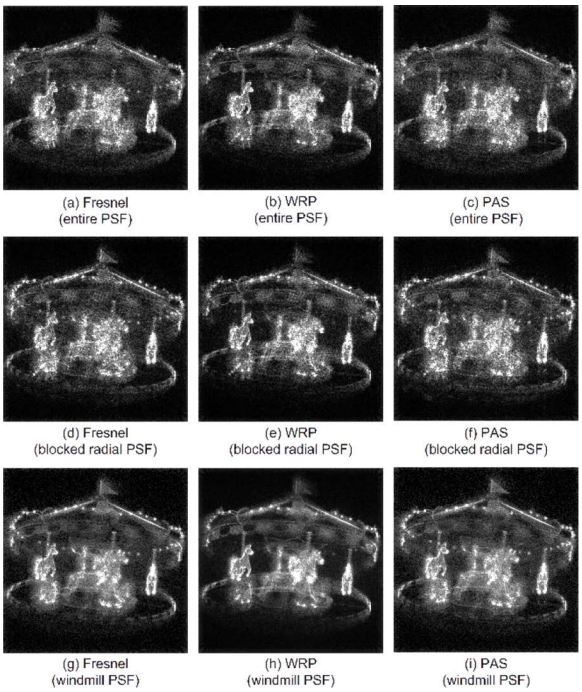

Fig. 8. Reconstructed images. (Object: Merry-go-round; reconstruction distance 11.28 cm from the CGHs). We adjusted the contrast to make it easier to see the reconstructed images.

Table 2. CGH calculation time.

	Calculation method	Earth		Merry-go-round	
		Calculation time [s]	Speed-up rate	Calculation time [s]	Speed-up rate
Entire PSF	Fresnel	201.8	1.0	676.9	1.0
	WRP	10.9	18.5	30.6	22.1
	PAS(B = 32, S = 128)	2.8	72.1	6.9	98.1
Blocked radial PSF	Fresnel	84.0	2.4	274.9	2.5
	WRP	6.4	31.5	15.8	42.8
	PAS(B = 32, S = 128)	2.1	96.1	4.0	169.2
Windmill PSF	Fresnel	86.1	2.3	282.0	2.4
	WRP	6.6	30.6	15.8	42.8
	PAS(B = 32, S = 128)	2.3	87.7	5.2	130.2

Table 3 shows the results of image-quality evaluations of the reconstructed images. We used the peak signal-to-noise ratio (PSNR) to evaluate the image quality. For the blocked radial PSF and the windmill PSF, the image quality is degraded compared to the entire PSF, but the PSNR remains above 30 dB. Table 3 shows that the reconstructed images can be observed from the front with little degradation even with the blocked radial PSF and the windmill PSF.

Next, we describe CGH calculations using RGB–D images. Figure 9 shows the RGB–D images used in this study (a Papillon and a Buddha) [38]. Table 4 shows the parameters of the CGH calculation. Each object was 2 cm thick, and the sampling interval in the depth direction was set to 0.2 mm. The depth image thus represented the depth with 100 depth steps. We extracted pixels

Optics EXPRESS

Table 3. Image-quality evaluation of the reconstructed image.

	Calculation method	Earth	Merry-go-round
		PSNR[dB]	PSNR[dB]
	Fresnel	-	-
Entire PSF	WRP	37.4	44.6
	PAS(B = 32, S = 128)	44.7	51.9
	Fresnel	34.2	42.0
Blocked radial PSF	WRP	35.4	42.9
	PAS(B = 32, S = 128)	34.1	41.8
	Fresnel	34.6	42.5
Windmill PSF	WRP	35.0	42.2
	PAS(B = 32, S = 128)	34.4	42.0

Table 4. Calculation parameters for CGH.

Number of pixels	2,048 × 2,048 [pixels]
Pixel pitch	3.74 [μm]
Wavelength	Red: 633 [nm] Green: 532 [nm] Blue: 450 [nm]
Number of object Points	Papillon: 786,432 points Buddha: 786,432 points
Object thickness	2.0 [cm]
Distance to CGH	10.0[cm]
Distance to WRP	0.5 [cm]
Line size (L)	256 [pixel]
Block size (s)	32 × 32 [pixels]

from the RGB image corresponding to the pixels in the depth image, used them to generate the point-cloud data, and then used the point-cloud data to calculate the CGH.

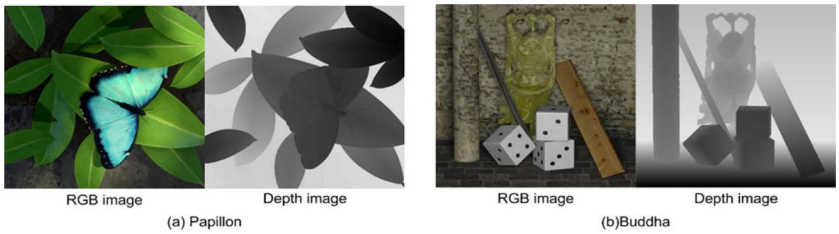

Fig. 9. Original RGB–D images [38].

Figures 10 and 11 show the images reconstructed from the CGHs using the entire PSF, the blocked radial PSF, and the windmill PSF. In this study, we multiplied the RGB images by a random phase. The reason for the use of random phases is as follows. We convert a complex amplitude hologram obtained from a hologram calculation into a phase-only hologram for simulation and optical reconstructions. Phase-only holograms requires that the object light distribution on the hologram plane is uniform. If random phase is not used, the light distribution

Optics EXPRESS

Fig. 10. Reconstructed images (Object: Butterfly; reconstruction distance 10.52 cm from the CGHs).

on the hologram plane will not be uniform, and the correct reconstructed image will not be obtained. By introducing a random phase, we have made the distribution of light on the hologram plane uniform, so that a correct reconstructed image can be obtained.

Table 5 shows the resulting calculation times, which is the sum of the CGH calculation time for the three separate colors. Table 5 shows that the blocked radial PSF and the windmill PSF can accelerate the CGH calculation even when using RGB–D images. In particular, when applied to the PAS algorithm, we achieved a speed up of more than 200 fold.

Table 6 shows the results of the image-quality evaluation of the reconstructed images. The reconstructed images can be observed from the front with little degradation even with the blocked radial PSF and the windmill PSF.

We next consider using the windmill PSF to expand the viewing angles of holograms. We used the PAS algorithm (B = 32, S = 64) for the calculations and the rotatin angle of 10° for the windmill PSF. Table 7 shows the parameters of the CGH calculation.

Figure 12 shows the images reconstructed from the CGHs created using each calculation method, as observed from an oblique angle of 2.0° horizontally and −1.0° vertically from the center of the CGH. Table 8 shows the results of the image-quality evaluation of the reconstructed images. Figure 12 shows that when images reconstructed using the blocked radial PSF were observed from an oblique direction, part of the image was missing. It contained additional noise, while the images reconstructed using the windmill PSFs were similar to those reconstructed using the entire PSF. The PSNR between the entire PSF and blocked radial PSF was 27.4, while the entire PSF and the windmill PSF was 31.5 higher than the former case.

Lastly, we show optical reconstructions using the entire PSF-based holograms and the windmill PSF-based holograms. We used a 532 nm laser, a Holoeye GAEA-2 as the SLM, and a Basler acA1300-30 g camera. The whole section marked in yellow in Fig. 13 was moved along the z-axis for the z-scan used for the 3D reconstruction. We used a rotating ground-glass plate to reduce

Optics EXPRESS

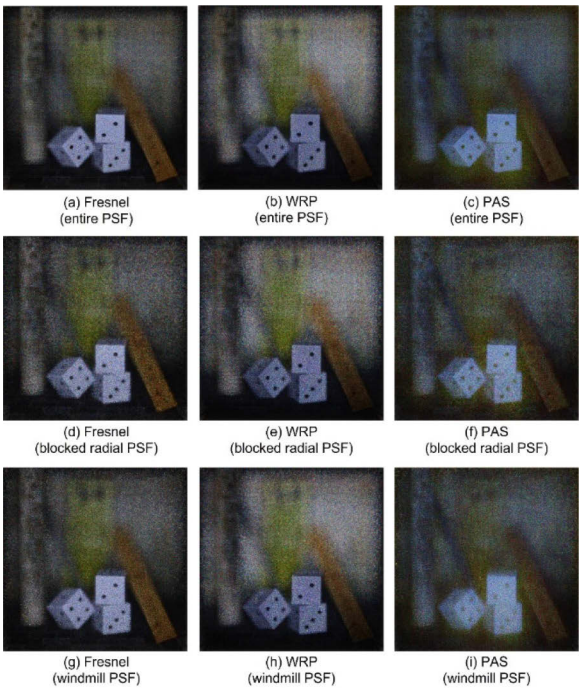

Fig. 11. Reconstructed images (Object: Buddha; reconstruction distance 10.42 cm from the CGHs).

Table 5. CGH calculation time. This calculation time is the sum of the CGH calculation times for the three colors.

	Calculation method	Butterfly		Buddha	
		Calculation time [s]	Speed-up factor	Calculation time [s]	Speed-up factor
Entire PSF	Fresnel	5878.7	1.0	5757.2	1.0
	WRP	217.1	27.1	257.4	22.4
	PAS(B = 32, S = 128)	36.3	161.9	39.8	144.7
Blocked radial PSF	Fresnel	2675.3	2.2	2565.4	2.2
	WRP	111.4	52.8	128.9	44.7
	PAS(B = 32, S = 128)	26.1	225.2	27.8	207.1
Windmill PSF	Fresnel	2628.8	2.2	2661.3	2.2
	WRP	112.3	52.3	128.6	44.8
	PAS(B = 32, S = 128)	28.3	207.7	28.7	200.6

speckle noise. The experimental exposures were made with 33 ms exposure times, minimal gain, and gamma = 1.0.

Figures 14 and 15 show the experimental results for the Earth and butterfly objects, which were obtained 100 to 120 mm behind the SLM. The holograms were calculated using Fresnel hologram calculations of Eq. (1) with the entire PSF and using PAS with the windmill PSF. The image quality is almost equivalent for all the reconstructed images. In other words, we show that

Optics EXPRESS

Table 6. Image-quality evaluation of the entire reconstructed image.

	Calculation method	Butterfly	Buddha
		PSNR [dB]	PSNR [dB]
Entire PSF	Fresnel	-	-
	WRP	31.8	27.1
	PAS(B = 32, S = 128)	32.5	30.6
Blocked radial PSF	Fresnel	32.2	30.4
	WRP	31.5	26.9
	PAS(B = 32, S = 128)	32.3	30.5
Windmill PSF	Fresnel	32.3	30.5
	WRP	31.6	27.1
	PAS(B = 32, S = 128)	32.2	30.4

Table 7. Calculation parameters for CGH.

Number of pixels	8,192 × 8,192
Pixel pitch	3.74 μm
Wavelength	532 nm
Object Points	Earth: 99,330
Distance to CGH	50.0 cm

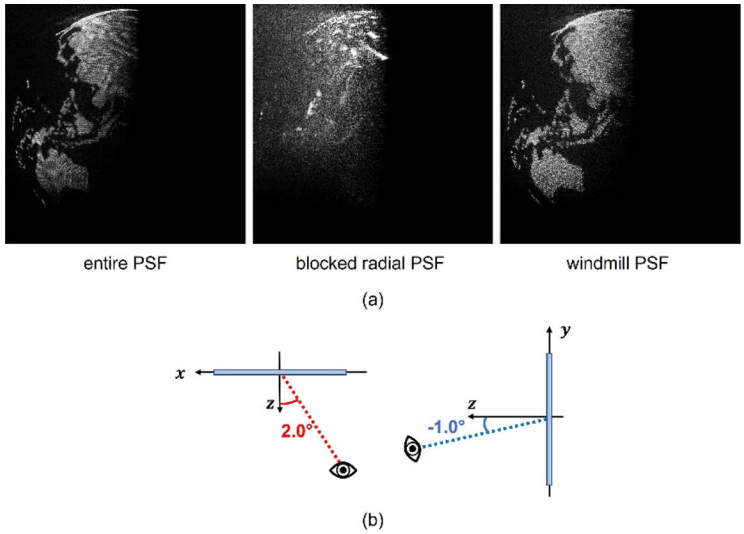

Fig. 12. Reconstructed images observed from an oblique angle: (a) reconstructed images using the entire, blocked radial and windmill PSFs, and (b) schematic diagram of the viewing position.

Optics EXPRESS

Table 8. Image-quality evaluation.

	Fig. 10
	FigurePSNR [dB]
Entire PSF	-
Blocked radial PSF	27.4
Windmill PSF	31.5

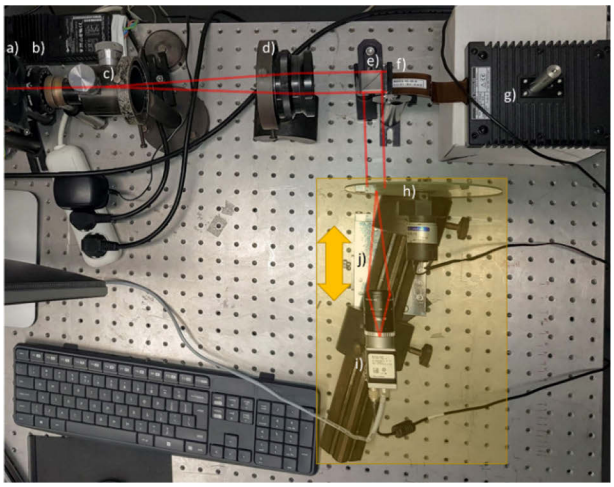

Fig. 13. Optical setup: (a) 532 nm laser, (b) half-wave plate, (c) pinhole, (d) lens, (e) beam splitter, (f) Holoeye GAEA-2, (g) SLM driver via HDMI 2.0, (h) rotating ground-glass plate, (i) Basler camera acA1300-30gc, and (j) motion stage.

the reconstructed images using different PSFs of the entire PSF and windmill PSF have similar depth of focus.

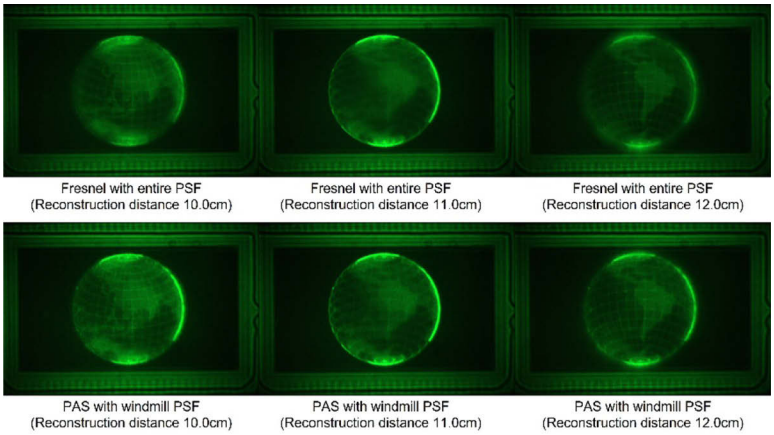

Fig. 14. Optically reconstructed images using Fresnel hologram calculations of Eq. (1) with the entire PSF (top row, Visualization 1) and using PAS with the windmill PSF (bottom row, Visualization 2).

Optics EXPRESS

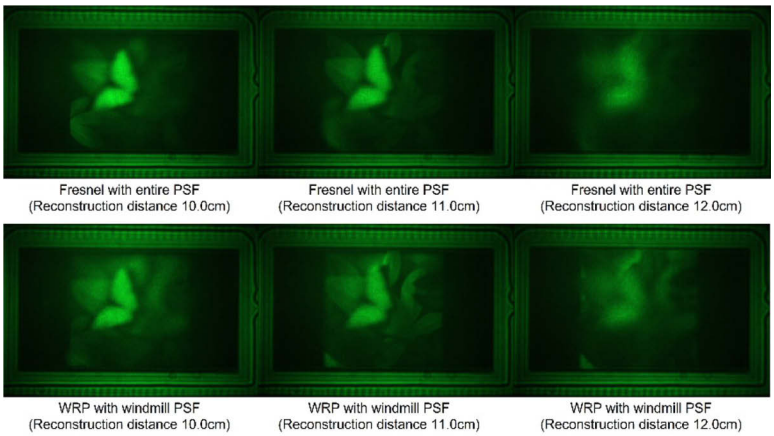

Fig. 15. Optically reconstructed images using Fresnel hologram calculations of Eq. (1) with the entire PSF (top row, Visualization 3) and using PAS with the windmill PSF (bottom row, Visualization 4).

4. Conclusions

The radial PSFs we proposed in a previous study [16] can contribute to speeding up CGH computations by reducing the amount of information from the amount contained in the entire PSF. However, they can only be used for near-eye displays where the eye position is fixed. However, it is difficult to use these radial PSFs with algorithms that compute CGHs by dividing them into blocks, such as the PAS algorithm. Therefore, in this study, we have proposed a blocked radial PSF that can be employed easily with such speed-up algorithms and a windmill PSF that can be applied to holographic displays with wide viewing angles. The blocked radial PSF can further speed-up conventional acceleration algorithms. The windmill PSF can expand the viewing area by rotating the blocked radial PSFs while maintaining the speed up of the CGH computations.

Funding. Japan Society for the Promotion of Science (JPJSBP120202302, 19H01097, 19H04132); CB POB FOTECH of Warsaw University of Technology within the Excellence Initiative: Research University (IDUB) programme; the joint JSPS-FWO scientific cooperation program (VS07820N); Fonds Wetenschappelijk Onderzoek (junior postdoctoral fellowship (12ZQ220N)).

Acknowledgments. This work was partially supported by JSPS KAKENHI Grant Numbers 19H04132 and 19H01097, The Research Foundation-Flanders also funded this research (FWO), junior postdoctoral fellowship (12ZQ220N), the joint JSPS-FWO scientific cooperation program (VS07820N), CB POB FOTECH of Warsaw University of Technology within the Excellence Initiative: Research University (IDUB) programme, and the Japan Society for the Promotion of Science (JPJSBP120202302). We are grateful to Dr. Hirotaka Nakayama for providing us with 3D object data.

Disclosures. The authors declare no conflicts of interest.

Data availability. Data underlying the results presented in this paper are not publicly available but may be obtained from the authors upon reasonable request.

References

1. T. -C. Poon and J. -P. Liu, "Introduction to modern digital holography: with MATLAB," Cambridge University Press (2014).
2. P. W. M. Tsang and T. C. Poon, "Review on the state-of-the-art technologies for acquisition and display of digital holograms," IEEE Trans. Ind. Informat. **12**(3), 886–901 (2016).
3. T. Shimobaba and T. Ito, "Computer Holography: Acceleration Algorithms and Hardware Implementations," CRC press (2019).
4. M. Lucente, "Interactive computation of holograms using a look-up table," J. Electron. Imag. **2**(1), 28–34 (1993).
5. S. –C. Kim and E. –S. Kim, "Effective generation of digital holograms of three-dimensional objects using a novel look-up table method," Appl. Opt. **47**(19), D55–D62 (2008).

Optics EXPRESS

6. Y. Pan, X. Xu, S. Solanki, X. Liang, R. B. A. Tanjung, C. Tan, and T.-C. Chong, "Fast CGH computation using S-LUT on GPU," Opt. Express **17**(21), 18543–18555 (2009).
7. S. Jiao, Z. Zhuang, and W. Zou, "Fast computer generated hologram calculation with a mini look-up table incorporated with radial symmetric interpolation," Opt. Express **25**(1), 112–123 (2017).
8. T. Shimobaba, N. Masuda, and T. Ito, "Simple and fast calculation algorithm for computer-generated hologram with wavefront recording plane," Opt. Lett. **34**(20), 3133–3135 (2009).
9. T. Yamaguchi and H. Yoshikawa, "Computer-generated image hologram," Chin. Opt. Lett. **9**(12), 120006 (2011).
10. T. Nishitsuji, T. Shimobaba, T. Kakue, and T. Ito, "Fast calculation of computer-generated hologram using run-length encoding based recurrence relation," Opt. Express **23**(8), 9852–9857 (2015).
11. M. Yamaguchi, H. Hoshino, T. Honda, and N. Ohyama, "Phase-added stereogram: calculation of hologram using computer graphics technique," Proc. SPIE **1914**, 25–31 (1993).
12. H. Kang, T. Yamaguchi, H. Yoshikawa, S.-C. Kim, and E.-S. Kim, "Acceleration method of computing a compensated phase-added stereogram on a graphic processing unit," Appl. Opt. **47**(31), 5784–5789 (2008).
13. D. Blinder and P. Schelkens, "Accelerated computer generated holography using sparse bases in the STFT domain," Opt. Express **26**(2), 1461–1473 (2018).
14. D. Blinder, "Direct calculation of computer-generated holograms in sparse bases," Opt. Express **27**(16), 23124–23137 (2019).
15. D. Blinder and P. Schelkens, "Phase added sub-stereograms for accelerating computer generated holography," Opt. Express **28**(11), 16924–16934 (2020).
16. D. Yasuki, T. Shimobaba, M. Makowski, J. Suszek, T. Kakue, and T. Ito, "Hologram computation using the radial point spread function," Appl. Opt. **60**(28), 8829–8837 (2021).
17. K. Matsushima and S. Nakahara, "Extremely high-definition full-parallax computer-generated hologram created by the polygon-based method," Appl. Opt. **48**(34), H54–H63 (2009).
18. Y.-P. Zhang, F. Wang, T.-C. Poon, S. Fan, and W. Xu, "Fast generation of full analytical polygon-based computer-generated holograms," Opt. Express **26**(15), 19206–19224 (2018).
19. F. Wang, T. Shimobaba, Y. Zhang, T. Kakue, and T. Ito, "Acceleration of polygon-based computer-generated holograms using look-up tables and reduction of the table size via principal component analysis," Opt. Express **29**(22), 35442–35455 (2021).
20. M.-S. Kim, G. Baasantseren, N. Kim, and J.-H. Park, "Hologram Generation of 3D Objects Using Multiple Orthographic View Images," J. Opt. Soc. Korea **12**(4), 269–274 (2008).
21. K. Wakunami and M. Yamaguchi, "Calculation for computer generated hologram using ray-sampling plane," Opt. Express **19**(10), 9086–9101 (2011).
22. Y. Ichihashi, R. Oi, T. Senoh, K. Yamamoto, and T. Kurita, "Real-time capture and reconstruction system with multiple GPUs for a 3D live scene by a generation from 4 K IP images to 8 K holograms," Opt. Express **20**(19), 21645–21655 (2012).
23. Y. Takaki and K. Ikeda, "Simplified calculation method for computer-generated holographic stereograms from multi-view images," Opt. Express **21**(8), 9652–9663 (2013).
24. N. Okada, T. Shimobaba, Y. Ichihashi, R. Oi, K. Yamamoto, M. Oikawa, T. Kakue, N. Masuda, and T. Ito, "Band-limited double-step Fresnel diffraction and its application to computer-generated holograms," Opt. Express **21**(7), 9192–9197 (2013).
25. J.-S. Chen and D. P. Chu, "Improved layer-based method for rapid hologram generation and real-time interactive holographic display applications," Opt. Express **23**(14), 18143–18155 (2015).
26. Y. Zhao, L. Cao, H. Zhang, D. Kong, and G. Jin, "Accurate calculation of computer-generated holograms using angular-spectrum layer-oriented method," Opt. Express **23**(20), 25440–25449 (2015).
27. R. Horisaki, R. Takagi, and J. Tanida, "Deep-learning-generated holography," Appl. Opt. **57**(14), 3859–3863 (2018).
28. H. Goi, K. Komuro, and T. Nomura, "Deep-learning-based binary hologram," Appl. Opt. **59**(23), 7103–7108 (2020).
29. J. Lee, J. Jeong, J. Cho, D. Yoo, B. Lee, and B. Lee, "Deep neural network for multi-depth hologram generation and its training strategy," Opt. Express **28**(18), 27137–27154 (2020).
30. L. Shi, B. Li, C. Kim, P. Kellnhofer, and W. Matusik, "Towards real-time photorealistic 3D holography with deep neural networks," Nature **591**(7849), 234–239 (2021).
31. K. Wakunami, P.-Y. Hsieh, R. Oi, T. Senoh, H. Sasaki, Y. Ichihashi, M. Okui, Y.-P. Huang, and K. Yamamoto, "Projection-type see-through holographic three-dimensional display," Nat. Commun. **7**(1), 12954 (2016).
32. E. Murakami, Y. Oguro, and Y. Sakamoto, "Study on compact head-mounted display system using electro-holography for augmented reality," IEICE Trans. Electron. **E100.C**(11), 965–971 (2017).
33. M. Makowski, R. Trybus, S. Fiderkiewicz, and J. Starobrat, "Overcoming the limitations of spatial light modulators for holographic near-eye displays," Optics and Photonics International Congress (OPIC) (2020).
34. E. Moon, M. Kim, J. Roh, H. Kim, and J. Hahn, "Holographic head-mounted display with RGB light emitting diode light source," Opt. Express **22**(6), 6526–6534 (2014).
35. A. Maimone, A. Georgiou, and J. S. Kollin, "Holographic near-eye displays for virtual and augmented reality," ACM Trans. Graph. **36**(4), 1–16 (2017).
36. T. Yoneyama, E. Murakami, Y. Oguro, H. Kubo, K. Yamaguchi, and Y. Sakamoto, "Holographic head-mounted display with correct accommodation and vergence stimuli," Opt. Eng. **57**(6), 061619 (2018).

Optics EXPRESS

37. Z. He, X. Sui, G. Jin, and L. Cao, "Progress in virtual reality and augmented reality based on holographic display," Appl. Opt. **58**(5), A74–A81 (2019).
38. S. Wanner, S. Meister, and B. Goldluecke, "Datasets and benchmarks for densely sampled 4d light fields," In VMV, 225–226 (2013).